Lattice dynamics of piezoelectric copper metaborate CuB_2O_4

R. V. Pisarev,[1] K. N. Boldyrev,[2] M. N. Popova,[2] A. N. Smirnov,[1] V. Yu. Davydov,[1] L. N. Bezmaternykh,[3] M. B. Smirnov,[4] and V. Yu. Kazimirov[5]

[1]*Ioffe Physical-Technical Institute, Russian Academy of Sciences, 194021 St. Petersburg, Russia*
[2]*Institute of Spectroscopy, Russian Academy of Sciences, 142190 Moscow, Troitsk, Russia*
[3]*Institute of Physics, Siberian Branch, Russian Academy of Sciences, 660036 Krasnoyarsk, Russia*
[4]*Physics Department, St. Petersburg State University, 199034 St. Petersburg, Russia*
[5]*Joint Institute for Nuclear Research, 141980 Dubna, Russia*

(Received 15 April 2013; published 8 July 2013)

Tetragonal piezoelectric copper metaborate CuB_2O_4 (space group $I\bar{4}2d$, $Z = 12$) became a subject of active research during the last decade because it demonstrates unique magnetic, optical, and magnetooptical properties. We report results of the optical studies of polarized infrared reflection and transmission spectra and Raman back-scattering spectra in the range from 20 to 2500 cm^{-1}. In accordance with the symmetry analysis, infrared studies allowed us to identify all polar $B_2(z)$, and $E(x,y)$ normal vibrational modes. Frequencies of all longitudinal (LO) and transverse (TO) optical phonons were determined by fitting the observed infrared reflection spectra. Raman measurements revealed the frequencies of the majority of nonpolar $A_1(xx,yy,zz)$ and $B_1(xx,yy)$ modes and polar $B_2(z)$ and $E(x,y)$ LO modes. We show that several groups of closely spaced spectral lines observed in the vibrational spectra of CuB_2O_4 can be considered as a result of the Davydov splitting, which takes place in the case of several equivalent molecular units in a primitive crystal cell. Multiphonon absorption in the range of 1200–2500 cm^{-1} was analyzed and a tentative assignment of some features was given. *Ab initio* calculations of all zone-center polar and nonpolar modes were performed using density functional theory (DFT). The computed frequency distribution is in a good agreement with observed line positions in the infrared and Raman spectra. All these results allowed us to suggest reliable identification of all zone-center phonon modes thus providing a firm basis for further experimental and theoretical studies of this material with complex crystal, magnetic, and electronic structures and fascinating physical properties.

DOI: 10.1103/PhysRevB.88.024301 PACS number(s): 63.20.−e, 78.30.−j, 63.20.dk

I. INTRODUCTION

Many of copper compounds exhibit exotic behaviors, and during the last decade, a copper metaborate CuB_2O_4 has become one of the most actively studied materials. Though it is known for quite a long time,[1] its crystal structure was solved only in 1971 and refined later.[2,3] Quite recently, CuB_2O_4 was found as a mineral in a Chile mine and was named santarosaite.[4] From the crystallographic and chemical point of view, this unique material is characterized by a large unit cell, complex crystal and magnetic structures, and several phase transitions at low temperatures. It is one of a few known examples where twelve copper Cu^{2+} ions ($3d^9$ outer shell, $S = 1/2$) in the unit cell occupy two crystallographically distinct positions (see detailed discussion in Sec. II), and interaction between them leads to several interesting physical properties markedly different from those in other cuprates.[5–17] At low temperatures below $T_N = 21$ K, CuB_2O_4 shows an antiferromagnetic ordering and a rich magnetic phase diagram with several phase transitions. Commensurate and incommensurate magnetic structures are observed as a result of intra-sublattice and inter-sublattice mutual interactions.

Along with interesting magnetic, acoustic, dielectric, and other properties, this material demonstrates a rich variety of linear and nonlinear optical and magnetooptical properties. The absorption spectrum in the visible range, related to the crystal field split *d-d* transitions, was first reported in Ref. 18 and discussed in more detail recently.[19] Several recent publications reported unusual phenomena of magnetic-field-induced optical chirality and magnetoelectric dichroic signals.[20,21] However, these reports were followed by a strict symmetry analysis of observed magnetooptical phenomena,[22] which raised a conflicting "Comment-Reply" dispute in which the main arguments inevitably involved analysis of the macroscopic crystal symmetry, magnetic symmetry, and the microscopic nature of electronic transitions in copper metaborate.[23,24] Another example of an interesting optical property is the spectroscopic observation of crystallographic and magnetic-field-induced second harmonic generation in CuB_2O_4.[16,25–27] One more example of interest to optical properties of copper borates is a recent paper on CuB_2O_4 and $Cu_3B_2O_6$ in which the photocatalytic behavior of intrinsic electronic *d-d* midgap states in the visible spectral range was studied for a better understanding of the process of water splitting.[28]

The study of low-temperature optical absorption spectra and second harmonic generation spectra allowed assignment of six zero-phonon (ZP) lines related to electronic transitions between crystal-field-split levels within two different 4*b* and 8*d* copper sublattices.[19,25] Each of these ZP lines in the range of 11 000–19 000 cm^{-1} (1.4–2.4 eV) is followed by an exceptionally rich vibronic structure covering the full range of phonon frequencies up to 1200 cm^{-1}. Such a rich structure when phonon sidebands are observed at *all* six ZP lines is quite unique for the 3*d* compounds. We did not succeed in finding any similar example in the literature. Evidently, no analysis of these rich vibronic structures could be done without a detailed knowledge of the lattice dynamics, which is replicated in phonon frequencies over the entire Brillouin

zone. This task is complicated by the large unit cell of CuB_2O_4 ($Z = 12$), which results in the expected total number of 126 normal phonon modes, see symmetry analysis in Sec. II. To the best of our knowledge, only a part of the unpolarized infrared phonon absorption spectrum in the range of 400–2000 cm^{-1} was reported without any analysis of the data and any list of phonon frequencies.[2,29] Evidently, these partial and qualitative data cannot be of any help for understanding the lattice dynamics and the exceptionally rich vibronic spectra of this unique compound. These arguments motivated the present experimental and theoretical study of lattice dynamics of copper metaborate.

In this paper, we report a detailed study of the polarized infrared reflection and absorption spectra and polarized Raman scattering spectra of copper metaborate CuB_2O_4. Symmetry analysis is done in order to classify infrared active transverse and longitudinal phonons and Raman active phonons. The experimental study allowed us to determine most of the phonons and their symmetries at the center of the Brillouin zone. Theoretical *ab initio* calculation of infrared and Raman active phonon frequencies was performed and results are discussed in relation to the experimental data.

The paper is organized as follows. In Sec. II, we analyze in detail the crystal structure emphasizing the characteristic structure elements. A symmetry analysis of the Raman and infrared active phonons is given. In Sec. III, we describe the experimental facilities used for the measurements of the infrared reflection and transmission spectra and Raman scattering spectra. The single-crystal growth and preparation of samples is briefly discussed. In Sec. IV, we consider the infrared spectra. The Raman scattering spectra are presented in Sec. V. In Sec. VI, the results of *ab initio* calculations of polar and nonpolar modes are given. In Sec. VII, we discuss the experimental and theoretical results, which are followed by conclusions and acknowledgements.

II. CRYSTAL STRUCTURE AND LATTICE MODES OF CuB_2O_4

A. Crystal structure and particular structure elements

Copper metaborate CuB_2O_4 crystallizes in a noncentrosymmetric tetragonal structure with the point group symmetry $\bar{4}2m$, the space group $I\bar{4}2d$ (No. 122).[2,3,5,30] The unit cell contains 12 formula units and the lattice parameters are $a = b = 11.484$ Å and $c = 5.620$ Å.[2] Slightly different values were given in Refs. 3 and 28. Figures 1 and 2 show different projections of the unit cell. The structure consists of a strongly coupled three-dimensional (3D) network of BO_4 tetrahedrons with cavities between them occupied by copper ions in the 4*b* and 8*d* positions. There are two types of boron atoms B1(16*e*) and B2(8*d*) positioned at the centers of tetrahedrons, and the bond lengths B-O vary between 1.444 and 1.487 Å. The tetrahedrons BO_4 are shown in Figs. 1 and 2 by dark-blue (B1) and cyan (B2) colors. All tetrahedrons are linked by common oxygen ions. There are four nonequivalent oxygen ions in the unit cell, O1(16*e*), O2(8*d*), O3(8*d*), and O4(16*e*).[2,30]

An interesting feature of the 3D boron-tetrahedron network is a formation of spiral chains twisting in the direction of the *c* axis. These helixes are divided into $3(BO_4)$ and $4(BO_4)$ groups, which are shown in Fig. 2 by blue and cyan colors, respectively. The combination of two $3(BO_4)$ and two 4(BO4) spirals forms groups of triple spirals. In each group, the sign of spiral twisting of $3(BO_4)$ and $4(BO_4)$ tetrahedrons is opposite. Namely, if the sign of $3(BO_4)$ twisting is right-handed, then the sign of $4(BO_4)$ twisting is left-handed, and vice versa. The unit cell contains two inequivalent groups with opposite sign of twisting, which in accordance with the point group symmetry $\bar{4}2m$ are transformed to each other by the symmetry operation $S_4(\bar{4})$. The spiral groups are linked between each other by rings composed of three (BO_4) tetrahedrons, which can be seen in Fig. 2.

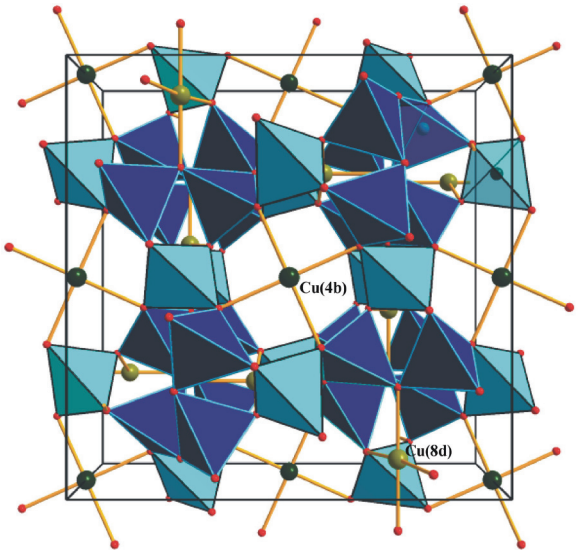

FIG. 1. (Color online) Three-dimensional view of the unit cell of CuB_2O_4 along the *z* axis. The $B1O_4$ and $B2O_4$ tetrahedrons are shown by dark blue and cyan colors, respectively. Brown lines represent Cu-O bonds.

Other interesting features of the CuB_2O_4 structure are the broad tunnels formed by the 8-element rings at the centers of which are 4*b* copper Cu^{2+} ions. These 4*b* ions are linked by four short Cu(4*b*)-O1 bonds (1.9988 Å) to the (BO_4) rings. The angles between these bonds are close to 90°. Besides these short bonds, the 4*b* copper ions are linked by longer bonds of 2.864 Å to the apexes of almost ideal $[Cu(4b)][O4]_4$ squares.

The 8*d* copper Cu^{2+} ions are also positioned at the centers of the eight-element rings, which are more difficult to see. Their planes are parallel to the (xz) and (yz) planes as can be seen in Fig. 1. There are rings formed by the B1-O3-B1-O1-B2-O4-B1-O3-B1-O2-B1-O3-B1-O4-B2-O1 chains. The 8*d* copper Cu^{2+} ions at the centers of these rings form four short Cu-O bonds. These bonds are the Cu(8*d*)-O3 of 1.8857 Å, Cu(8*d*)-O2 of 1.9029 Å, and two bonds Cu(8*d*)-O4 with the length of 1.9810 Å, and the angles between the bonds are close to 90°. Thus regardless of the difference in the formal symmetry of the 4*b* and 8*d* positions of Cu^{2+}, namely, S_4 for 4*b* ions and C_2 for the 8*d* ions, in both of them, Cu^{2+} ions are at the centers of almost ideal planar squares. Each 8*d* copper Cu^{2+} ion is linked by six long bonds directed to the apexes of distorted octahedra $[Cu(8d)][O1]_4[O3]_2$. These six long bonds are two bonds of 2.939 Å with O1, two bonds of 3.067 Å with O3, and two bonds of 3.070 Å (with O1).

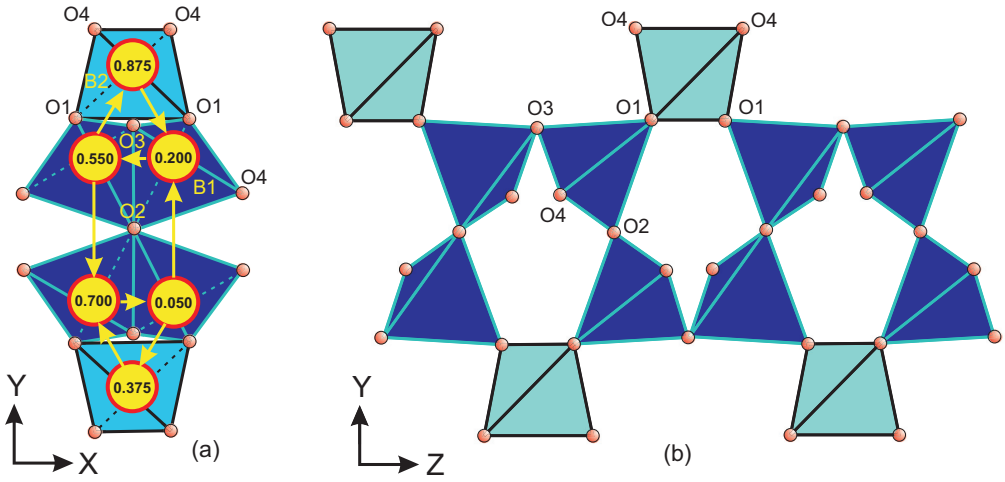

FIG. 2. (Color online) (a) The (xy) and (b) (yz) projections of the CuB_2O_4 unit cell. Numbers in panel (a) indicate z positions of the boron atoms. Yellow arrows show orientations of the spiral links.

B. Symmetry analysis of the lattice modes

The primitive unit cell contains 42 atoms, which results in 126 normal modes. The group-theoretical analysis[31,32] gives the following set of the zone-center lattice modes:

$$126\Gamma = 13A_1 + 17A_2 + 14B_1 + 18B_2(T_z) + 32E(T_x, T_y). \tag{1}$$

After subtracting $B_2(T_z) + E(T_x, T_y)$ acoustic modes, we get 123 optical vibrational modes. Among them, A_2 modes are silent; the polar $B_2(T_z)$ and $E(T_x, T_y)$ modes are infrared active for $E(\omega)\|z$ and $E(\omega)\|x$ polarizations of the incident radiation, respectively. The Raman tensors for the relevant modes are

$$A_1: \begin{pmatrix} a & 0 & 0 \\ 0 & a & 0 \\ 0 & 0 & b \end{pmatrix}; \quad B_1: \begin{pmatrix} c & 0 & 0 \\ 0 & -c & 0 \\ 0 & 0 & 0 \end{pmatrix};$$

$$B_2: \begin{pmatrix} 0 & d & 0 \\ d & 0 & 0 \\ 0 & 0 & 0 \end{pmatrix}; \tag{2}$$

$$E_x: \begin{pmatrix} 0 & 0 & 0 \\ 0 & 0 & e \\ 0 & e & 0 \end{pmatrix}; \quad E_y: \begin{pmatrix} 0 & 0 & e \\ 0 & 0 & 0 \\ e & 0 & 0 \end{pmatrix}. \tag{3}$$

The characteristic structural groups of the CuB_2O_4 unit cell are BO_4 tetrahedrons, which form a 3D network with cavities occupied by $4b$ and $8d$ copper ions. Other characteristic groups are CuO_4 planar squares. In order to get a deeper insight into the lattice dynamics of copper metaborate, it is instructive to discuss in brief internal modes of these two groups.

C. Internal modes of BO_4 tetrahedrons

Internal modes of an isolated BO_4 tetrahedron possessing the T_d symmetry are shown in Fig. 3.[33] There are two triply degenerate F_2 vibrations ν_3 and ν_4, one doubly degenerate E vibration ν_2, and one nondegenerate totally symmetric A_1 vibration ν_1. The ν_3 mode at 950 cm^{-1} and the ν_1 mode at 747 cm^{-1} are related to the valent boron-oxygen B-O vibrations and have the highest frequencies. In the ν_3 mode, the boron atoms exhibit the largest displacements whereas in the ν_1 mode oxygen atoms oscillate with the largest amplitude, which explains the difference in the frequencies of the ν_3 and ν_1 modes. The triple degeneracy of the ν_3 mode is completely lifted by placing the BO_4 tetrahedron into each of the $16e$ or $8d$ positions in the crystal lattice. There are twelve BO_4 tetrahedrons per primitive cell. Correspondingly, the vibrational spectrum of CuB_2O_4 must contain 36 modes originating from the ν_3 vibration of an isolated BO_4 tetrahedron and, hence, having frequencies around 950 cm^{-1}. To get the symmetries of these crystal modes, we note, first, that the F_2 representation of the T_d point symmetry group (an isolated BO_4 tetrahedron) splits into $A + 2B$ representations of the C_2 point symmetry group for the $8d$ sites and into $3A$ representations of the C_1 point group for the $16e$ sites of the CuB_2O_4 crystal lattice. Then, by correlating the site symmetry group representations to those of the D_{2d} unit cell symmetry group, we take into account the presence of several BO_4 tetrahedrons within the unit cell interacting with each other[31] and find that the ν_3 vibration of an isolated BO_4 tetrahedron gives rise to the

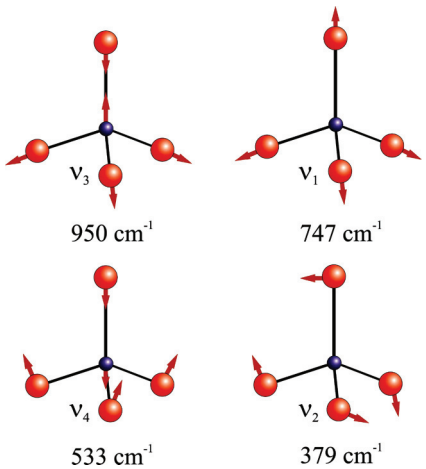

FIG. 3. (Color online) Normal vibrations and relevant frequencies of an isolated BO_4 tetrahedron.[33]

following crystalline modes at the Brillouin zone center:

$$36\nu(\mathrm{B}) = 4A_1 + 5A_2 + 4B_1 + 5B_2 + 9E. \quad (4)$$

A pulsation mode ν_1 involves a synchronous stretching of all B-O bonds due to motions of mainly oxygen atoms. In the crystal, there are twelve such modes positioned near 747 cm^{-1} and distributed by symmetry as follows:

$$12\nu(\mathrm{O}) = 2A_1 + 1A_2 + 2B_1 + 1B_2 + 3E. \quad (5)$$

In total, there are 48 high-frequency crystalline modes corresponding to valent B-O vibrations:

$$48\nu(\mathrm{B-O}) = 6A_1 + 6A_2 + 6B_1 + 6B_2 + 12E. \quad (6)$$

The ν_4 mode at 533 cm^{-1} and ν_2 mode at 379 cm^{-1} of an isolated BO_4 tetrahedron are related to the motions that change O-B-O and B-O-B valent angles. They induce 60 crystalline modes (36 modes originating from the ν_4 vibration and 24 modes arising from the ν_2 vibration) positioned at lower frequencies.

D. Internal modes of CuO_4 planar squares and the Davydov splitting

24 valent Cu(4*b*)-O and Cu(8*d*)-O bonds define the 24 frequencies of the modes below the frequency range of the B-O vibrations. According to symmetry rules, they are distributed as

$$24\nu(\mathrm{Cu\text{-}O}) = 4A_1 + 2A_2 + 4B_1 + 2B_2 + 6E. \quad (7)$$

The frequencies of these modes depend on what atom, Cu or O, is involved in a particular vibration. The first group of vibrations is mixed with ν(O) modes, whereas the second group of ν(Cu) vibrations possesses lower frequencies in the range of 400–500 cm^{-1}. By symmetry rules these modes are distributed as

$$15\nu(\mathrm{Cu}) = 1A_1 + 2A_2 + 2B_1 + 2B_2 + 4E. \quad (8)$$

Copper ions in CuB_2O_4 reside at the centers of almost regular CuO_4 planar squares, with their planes parallel to the (xy) plane for Cu(4*b*)O_4 and to the (xz) and (yz) planes for Cu(8*d*)O_4. There are two Cu(4*b*)O_4 units and four Cu(8*d*)O_4 units in a primitive crystallographic cell of CuB_2O_4. As all these units are well isolated one from another, not having common oxygen atoms, it seems appropriate to analyze their vibrations starting from the normal vibrational modes of "a free CuO_4 molecule" possessing the D_{4h} symmetry and, then, to trace a transformation of these modes into Davydov multiplets in the crystal. The group theoretical analysis gives the following normal modes of an isolated CuO_4 planar square:

$$15\Gamma = A_{1g} + A_{2g} + 2A_{2u} + B_{1g} + B_{1u} + B_{2g} + 3E_u + E_g. \quad (9)$$

Among them, $(A_{2u} + E_u)$ are pure translations and $(A_{2g} + E_g)$ are rotations.

When a CuO_4 unit is placed into a certain crystallographic position, the symmetry of vibrational modes changes in accordance with the local site symmetry; translations and rotations transform into translational and librational modes of the crystal, respectively. Interaction between several equivalent molecular units in the primitive cell results in the so-called

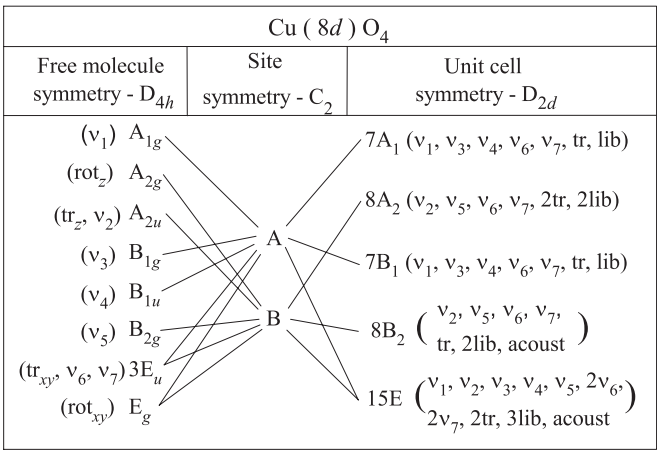

FIG. 4. Correlation scheme for the Cu(8*d*)O_4 group placed into the C_2 symmetry position of the CuB_2O_4 unit cell (D_{2d} symmetry).

Davydov multiplet in a crystal originating from a particular normal mode of a molecular unit.[34] In the case of weak interaction, the splitting is small and, analyzing the spectra, one finds lattice modes of different symmetries having close frequencies. The scheme in Fig. 4 illustrates, on the example of an isolated CuO_4 planar square placed into the $8d(C_2)$ position of the CuB_2O_4 crystal lattice, how a single molecular vibration transforms into a Davydov multiplet. By consulting the correlation scheme in Fig. 4, we get that each of the $A_{1g}(\nu_1)$, $B_{1g}(\nu_3)$, and $B_{1u}(\nu_4)$ vibrations splits into the $(A_1 + B_2 + E)$ Davydov triplet; the $A_{2u}(\nu_2)$ and $B_{2g}(\nu_5)$ vibrations deliver the $(A_2 + B_2 + E)$ Davydov triplet each; and the $E_u(\nu_6$ or $\nu_7)$ vibration transforms into the $(A_1 + A_2 + B_1 + B_2 + 2E)$ Davydov sextet. In addition, one $(A_2 + B_2 + E)$ triplet and one $(A_1 + A_2 + B_1 + B_2 + 2E)$ sextet correspond to librations; one more such combination described translational modes. In total, the following set of Davydov multiplets results from CuO_4 units in the 8*d* positions:

$$3(A_1 + B_1 + E) + 4(A_2 + B_2 + E) + 4(A_1 + B_1 + A_2 + B_2 + 2E). \quad (10)$$

Being placed into the $4b(S_4)$ positions of the D_{2d} unit cell, the CuO_4 quasimolecule delivers the following Davydov doublets:

$$3(A_1 + A_2) + 4(B_1 + B_2) + 4(E + E). \quad (11)$$

The doublets $(A_1 + A_2)$ and $(E + E)$ correspond to librational motions, but the doublets $(B_1 + B_2)$ and $(E + E)$ represent translational motions. All rest doublets are of purely vibrational nature.

III. EXPERIMENTAL AND COMPUTATIONAL DETAILS

Infrared (IR) reflection spectra at the nearly normal incidence (10°) and transmission spectra at normal incidence were registered in a broad spectral range using a Fourier-transform infrared spectrometer Bruker IFS 125HR. Helium-cooled bolometer for the far infrared spectral region (FIR, 10–500 cm^{-1}) and a liquid-nitrogen cooled MCT detector for the middle infrared spectral region (MIR, 400–3000 cm^{-1}) were used. Samples were measured, mainly, at room temperature.

Several transmission measurements at 6 K were performed using a closed-cycle helium cryostat Cryomech ST403. A wire-grid polarizer and a KRS-5 polarizer were used in the FIR and in the MIR spectral regions, respectively.

Raman scattering spectra were measured in the range of 20–1500 cm^{-1} with the use of a Jobin-Yvon spectrometer equipped with a cooled charge-coupled device (CCD) camera. An argon-laser line $\lambda = 514$ nm was used for the excitation. All measurements were done in the back-scattering reflection mode and multiple geometry/polarization settings were used such as $x(zz)\bar{x}$, $z(xx)\bar{z}$, $z(xy)\bar{z}$, $y(xx)\bar{y}$, $x(zy)\bar{x}$, etc. Several measurements were done in mixed polarizations, e.g., $z(x+y,y+x)\bar{z}$.

Large single crystals of about several cubic centimeters of good optical quality without any visually seen defects were grown by a Kyropulos method from the melt of B_2O_3, CuO, Li_2O, and MoO_3 oxides.[11] Plane-parallel polished plates of (010) and (001) orientation with thickness between 100 and 1000 μm were prepared from x-ray oriented single crystals. The precise orientation of the sample faces and crystallographic axes was an important factor to avoid mixing of modes in infrared and Raman measurements. In particular, samples of different orientations and thicknesses were used in Raman scattering experiments and the precise orientation of the x and y axes, and obviously the z axis, was important. Infrared reflection and transmission spectra were measured for (xz) samples with thickness of 784 and 104 μm. This approach, using samples of different orientations and thicknesses, allowed us to make a more reliable assignment of the observed modes and correlations between infrared and Raman scattering measurements, where it was possible.

Copper borate is optically uniaxial crystal and therefore is birefringent. As it is well known, in a general case, the birefringence can destroy the linear polarization making it elliptical, and therefore can lead to a mixing of modes in the infrared and Raman spectra. The refractive index n was evaluated earlier from reflectance measurements in the visible spectral range from an undetermined as-grown face of a single crystal and was found to be in the range of $n = 1.75$–1.77 (at photon energy 2.0 eV) and $n = 1.78$–1.80 (at 3.0 eV).[19] A close value $n = 1.75$ was recently reported for a mineral santarosaite identified as CuB_2O_4.[4] These values were used as starting values in the fitting procedure when analyzing the infrared reflectance data. Our data show that the expected linear birefringence is of the order of $\Delta n_{ac} = n_a - n_c \approx 10^{-2}$. Other values $n_g = 1.69$ and $n_p = 1.582$ were reported[35] which, on one hand, are lower than the values given above, and on the other hand, the birefringence in this case is notably higher. In Sec. IV, we show the values of the index of refraction evaluated from our infrared reflection measurements.

The density functional theory (DFT)[36–38] was applied to simulate the atomic structure and vibrational frequencies of CuB_2O_4. We discuss the results of the DFT calculations and use them for interpreting the experimental infrared and Raman spectra. The atomic orbital based DMol3-program[39] was employed for the *ab initio* calculations. The Perdew-Wang (PVC) exchange-correlation functional[40] in the local density approximation (LDA) was used. The DNP atomic basis[41] was applied to ensure high accuracy of computations. The DFT semicore pseudopotential method was chosen as a compromise between computational cost and accuracy of the simulations. A Monkhorst-Pack grid of $3\times3\times2$ points in the k space was used for the Brillouin zone sampling.

IV. INFRARED REFLECTION, TRANSMISSION AND MULTIPHONON ABSORPTION SPECTRA

A. Far infrared reflection and transmission spectra of CuB_2O_4

Figure 5 shows the room-temperature infrared reflection spectra of a CuB_2O_4 single crystal measured with the polarization of the incident light (a) parallel to the z axis $E(\omega)\|z$ and (b) parallel to the x axis $E(\omega)\|x$. These two measurements allowed us to probe the $B_2(z)$ and $E(x,y)$ polar optical modes, respectively. Experimental data are presented by solid lines. $12B_2$ and $18E$ modes are clearly observed as typically shaped features in the reflection spectra. We found that single crystals of CuB_2O_4 are well transparent below 200 cm^{-1}, however, as we show below, several weak phonons were detected in transmission measurements below 200 cm^{-1}.

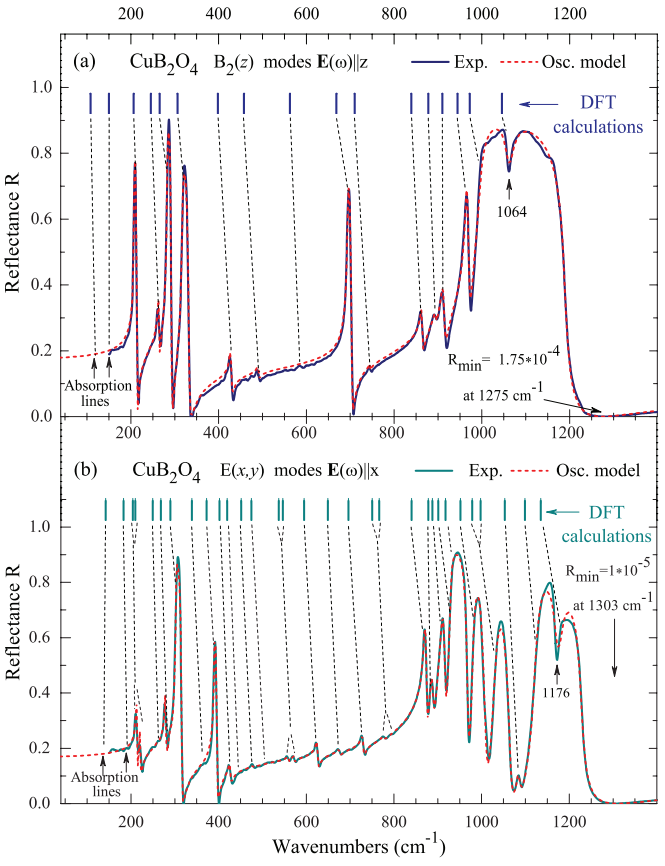

FIG. 5. (Color online) Reflection spectra of CuB_2O_4 measured with the polarization of the incident light (a) $E(\omega)\|z$ (solid marine line), which probes the polar $B_2(z)$ modes, and (b) $E(\omega)\|x$ (solid cyan line), which probes the polar $E(x,y)$ modes. Spectra are compared with fitting calculations (red dashed lines) based on a model of damped oscillators, see Eq. (13). Lines above the spectra show results of *ab initio* DFT calculations (see Sec. VI) of polar (a) $B_2(z)$ and (b) $E(x,y)$ modes. Frequencies of $B_2(z)$ and $E(x,y)$ modes evaluated from infrared and Raman experiments (Sec. V) are confronted in Tables I and II where results of DFT calculations (see Sec. VI) are presented numerically.

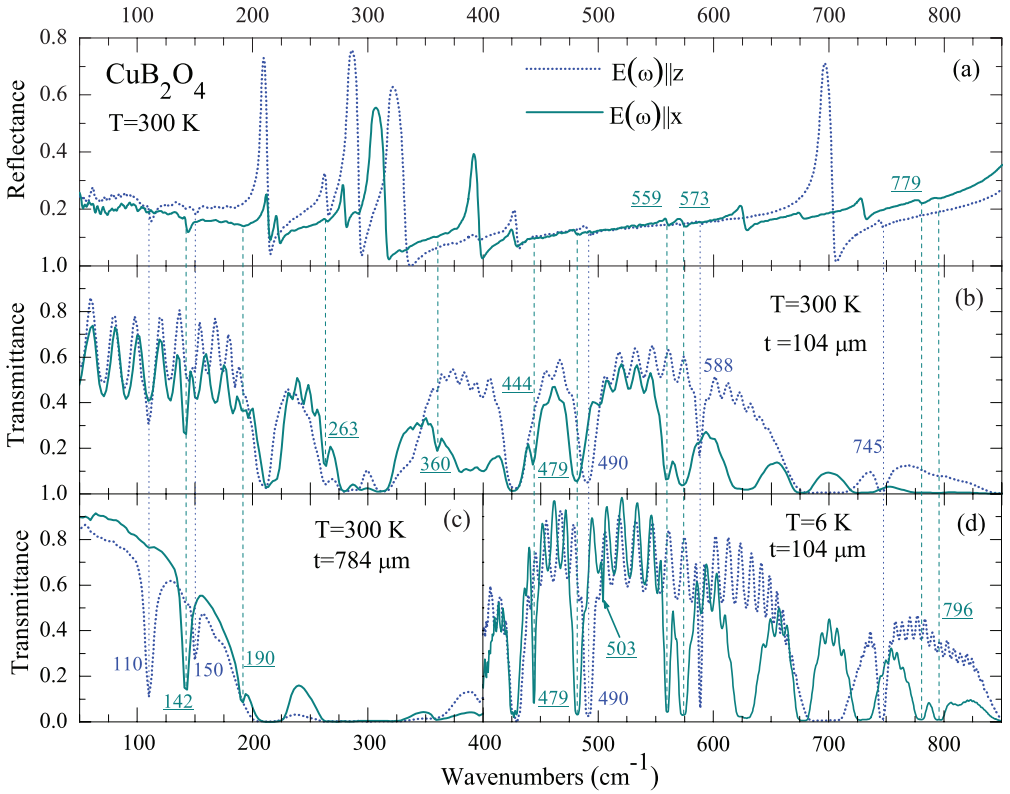

FIG. 6. (Color online) Comparison of the reflection (a) and transmission (b)–(d) spectra of CuB_2O_4 in the range of 50–850 cm^{-1}. The transmission spectra were measured using 104 and 784-μm (xz) samples at 6 and 300 K. Vertical cyan dashed lines for $E(\omega)\|x$ and blue dotted lines for $E(\omega)\|z$ indicate phonon modes for the two main polarizations, which are very weak or even unobservable in the reflection spectra. Interference in the transmission spectra is clearly seen in the regions of good transparency. Above 850 cm^{-1}, absorption was too high even in the 104-μm sample at $T = 6$ K and no measurements could be done.

Back-side reflection gives an additional contribution to the reflectance in both $E(\omega)\|z$ and $E(\omega)\|x$ polarizations. Weak phonon modes are observed as small dips in the reflectance spectra at 110 and 150 cm^{-1} for $E(\omega)\|z$ and 142 cm^{-1} for $E(\omega)\|x$. Additional dips are present on the tops of the strong highest-frequency reststrahlen bands in both polarizations, at 1064 cm^{-1} for $E(\omega)\|z$ and 1176 cm^{-1} for $E(\omega)\|x$, due to interference between a strong phonon and a weak one whose frequency is within the TO-LO splitting of the strong phonon.[42]

It was evident that reflection measurements provided us only with frequencies of sufficiently strong phonons. Thus, in order to unhide weak phonons, we have measured infrared transmission spectra, which are shown in Fig. 6. For a better comparison, Fig. 6(a) shows results of the reflection measurements. Transmission measurements have delivered an important information, namely, they clearly confirmed the presence of already mentioned weak phonons at 110, 150 [both for $E(\omega)\|z$], and 142 cm^{-1} [$E(\omega)\|x$]. Moreover, they have allowed us to reliably detect several more weak phonons, which were either not observed at all or observed as small peculiarities in the reflection spectra, see Fig. 5. Those are phonons with TO frequencies 490, 588, and 745 cm^{-1} in $E(\omega)\|z$ polarization, and phonons at 190, 263, 360, 444, 480, 503, 559, 573, 779, and 796 cm^{-1}, all in $E(\omega)\|x$ polarization. An interesting very weak phonon at 503 cm^{-1} indicated by an arrow in the bottom panel of Fig. 6(d) is observed as a very narrow absorption line with FWHM ≈ 1.1 cm^{-1} detected in the 104-μm thick sample only in the low-temperature transmission spectrum at $T = 6$ K. Evidently, such a phonon with very low oscillator strength could not be detected in reflection measurements but its existence was also confirmed by Raman scattering studies (see Table II and Fig. 13). The detailed study of the evolution of phonon spectra with temperature is out of the scope of the present work. We only note that while phonon frequencies show very small changes with lowering the temperature from 300 to 6 K, all phonon lines demonstrate a considerable narrowing, as a comparison of the middle (b) and lower, (c) and (d), panels in Fig. 6 shows.

For extracting the parameters of phonons that markedly contribute to the reflection spectra, we have performed the dispersion analysis using the REFFIT program.[43] The measured spectra were least-squares fitted by the spectra computed according to the expression

$$R(\omega) = \left| \frac{\sqrt{\varepsilon(\omega)} - 1}{\sqrt{\varepsilon(\omega)} + 1} \right|^2, \tag{12}$$

where the dielectric function $\varepsilon(\omega)$ was represented by the dispersion formula of J classical damped oscillators

$$\varepsilon(\omega) = \varepsilon_\infty + \sum_{j=1}^{J} \frac{f_j \omega_j^2}{\omega_j^2 - \omega^2 - i\gamma_j \omega}. \tag{13}$$

Here, ω_j are phonon frequencies, γ_j are damping constants, and f_j are oscillators strengths. Results of the fitting are presented by red dashed lines in Fig. 5. The fitting procedure has yielded the values $\varepsilon_{\infty\parallel} = 3.15 \pm 0.01$ and $\varepsilon_{\infty\perp} = 3.09 \pm 0.01$ for dielectric constants ε_∞ in Eq. (13), corresponding to the directions of polarization parallel and perpendicular to the z axis, respectively. These values allowed us to calculate $n_{\infty\parallel} = 1.775$ and $n_{\infty\perp} = 1.758$ with $\Delta n = 0.017$, which is consistent with $\Delta n = 0.02$ for the visible range data given in Sec. III.[19] From the interference pattern observed in the middle infrared (3800–6000 cm^{-1}) transmission spectra (not shown) of the 104-μm thick sample, dielectric constants for this frequency range were found according to the relation

$$\varepsilon(\omega) = n^2(\omega) = \left(\frac{1}{2t\Delta}\right)^2, \tag{14}$$

where n is the refractive index, t is the sample thickness, and Δ is the interval in cm^{-1} between the neighboring interference maxima. The obtained values $\varepsilon_{\infty\parallel} = 3.09 \pm 0.01$ and $\varepsilon_{\infty\perp} = 3.02 \pm 0.01$ correlate very well with those calculated from Eq. (13) using the parameters obtained from the fitting of the reflection data.

Tables I and II summarize the phonon parameters. Frequencies of longitudinal optical (LO) phonons were found as zeros of the dielectric function given by Eq. (13). Transverse TO frequencies of weak phonons are indicated as those obtained from the far infrared transmission spectra. All the 17B_2 modes and 30 of 31E modes were found from the infrared measurements. LO phonon frequencies observed in Raman scattering measurements (see Sec. V) are also included into Tables I and II, together with TO phonon frequencies found by *ab initio* DFT calculations (see Sec. VI). Correspondence between experimental and calculated frequencies is discussed in Sec. VI. Substituting the oscillator strengths from Tables I and II into Eq. (13), we find $\varepsilon_{0\parallel} = 6.06$ and $\varepsilon_{0\perp} = 5.77$ for static dielectric constants ($\omega = 0$), in good agreement with the values $\varepsilon_{0\parallel} = 6.05 \pm 0.10$ and $\varepsilon_{0\perp} = 5.76 \pm 0.10$ evaluated from the interference patterns observed in the 784-μm thick sample in the spectral range of (15–80 cm^{-1}) where copper metaborate is transparent (not shown).

As it was mentioned in Introduction, only a part of the unpolarized infrared phonon absorption spectrum in the range from 400 to 1600–2000 cm^{-1} was reported without any list of phonon frequencies or any analysis of the data.[2,29] Nevertheless, we can, at least qualitatively, compare the most prominent spectral features in these unpolarized spectra with our results evaluated from polarized reflection and transmission spectra (see Tables I and II). The spectra in these two papers are similar though differ in some details. In both papers, a well defined absorption band was reported at ≈425 cm^{-1}, which can be confronted with the $B_2(z)$ TO

TABLE I. Room-temperature parameters of the polar $B_2(z)$ modes found from the infrared spectra, Raman spectra, and *ab initio* DFT calculations. Frequencies ω_j, damping constants γ_j, and oscillator strengths f_j were found from infrared spectra using the Lorentz model of attenuated oscillators according to Eq. (13). $\varepsilon_{0\parallel} = 6.06$ and $\varepsilon_{\infty\parallel} = 3.15$ (see text).

	Frequency ω_j(cm^{-1})					
j	Raman	IR(LO)	IR(TO)	DFT(TO)	f_j	γ_j(cm^{-1})
1	110	. . .	110[a]	108	. . .	. . .
2	150	. . .	150[a]	149.9	. . .	. . .
3	213	214	207.7	206.5	0.411	1.3
4	265	265	263.2	245.6	0.108	3.2
5	292	293	282.6	265.6	0.470	1.4
6	333	333	317.0	306.2	0.336	3.4
7	430	430	427.7	398.4	0.038	4.5
8	491	491	490.5	457.5	0.009	4.0
9	588	. . .	587.9[a]	562.6	. . .	. . .
10	703	703	693.9	668.4	0.166	3.1
11	745	745.5	744.8	710.1	0.002	2.0
12	865	865	863.1	839.3	0.036	5.0
13	894	895	894.2	878.0	0.034	5.5
14	913	915	911.4	909.7	0.092	8.1
15	973	972	963.9	944.4	0.295	4.8
16	1192	1189	995.9	972.6	0.905	15.4
17	1060	. . .	1063.8	1045.8	0.025	23.6

[a]Observed in transmission spectra.

TABLE II. Room-temperature parameters of the polar $E(x,y)$ modes found from the far infrared spectra, Raman spectra, and *ab initio* DFT calculations. $\varepsilon_{0\perp} = 5.77$ and $\varepsilon_{\infty\perp} = 3.09$ (see text). ("sh" stands for shoulder.)

	Frequency ω_j(cm^{-1})					
j	Raman	IR(LO)	IR(TO)	DFT(TO)	f_j	γ_j(cm^{-1})
1	142	. . .	142.0[a]	142.3	. . .	. . .
2	190	. . .	190.0[a]	182.9	. . .	. . .
3	213	213.5	212.4	204.4	0.123	2.4
4	222	222	221.0	210.0	0.069	2.8
5	263	. . .	263.1[a]	249.7	0.004	1.4
6	283	280	278.8	268.3	0.108	2.3
7	318	316.5	302.2	290.1	0.428	1.5
8	359	. . .	360.0[a]	339.2	. . .	. . .
9	397	397	390.0	372.6	0.161	2.7
10	427	427	426.1	402.1	0.020	4.3
11	443	. . .	444.0[a]	419.6	. . .	. . .
12	480	. . .	479.6[a]	451.3	0.001	2.0
13	503	. . .	503.0[a,b]	474.8	. . .	. . .
14	560	. . .	558.9[a]	537.1	0.003	2.4
15	573	. . .	573.0[a]	546.4	0.005	3.5
16	627	628	625.0	595.1	0.042	4.9
17	676	677	676.2	649.1	0.006	5.0
18	729	730	729.3	696.4	0.018	4.5
19	778	. . .	778.8[a]	750.6	0.005	5.8
20	796[sh]	. . .	796.0[a]	766.4	. . .	. . .
21	876	875.5	869.8	840.5	0.244	4.7
22	890	890	886.2	878.6	0.121	7.7
23	915[sh]	917	908.3	887.9	0.417	8.2
24	969	969	929.0	901.4	0.440	5.3
25	993	. . .	. . .	917.9	. . .	. . .
26	1013	1009	979.4	951.9	0.100	9.3
27,28	1066	1065	1027.9	978.7,998.0	0.106	15.8
29	. . .	1086	1083.0	1052.8	0.013	11.0
30	1228	1227	1122.3	1098.8	0.182	13.2
31	. . .	. . .	1176.5	1135.0	0.011	25.0

[a]Observed in transmission spectra.
[b]Observed at 6 K.

mode at 427.7 cm^{-1} (see Table I and Fig. 6) and $E(x,y)$ TO mode at 426.1 cm^{-1} (see Table II and Fig. 6). Another well resolved intense feature[2,29] at ≈695 cm^{-1} can be compared with the $B_2(z)$ TO mode at 693.9 cm^{-1} (see Table I). The most intense broad absorption bands were observed in the range from 850 to 1200 cm^{-1}, which is exactly the range of the strongest phonons observed in our reflection spectra in both polarizations of the incident light, see Fig. 5. The strongest absorption feature in this spectral range[2,29] is at ≈946 cm^{-1}, which can be correlated with overlap of the $E(x,y)$ TO mode at 929.0 cm^{-1} (see Table II and Fig. 5) and the $B_2(z)$ TO mode at 963.9 cm^{-1} (see Table I). One more example is the highest frequency intense absorption band at ≈1128 cm^{-1}, which is consistent with the $E(x,y)$ TO mode at 1122.3 cm^{-1} in Table II. We restrict this confrontation by the given examples.

B. Multiphonon absorption spectra of CuB_2O_4

Figure 7 shows infrared absorption spectra of the 104 μm thick sample at 300 and 6 K, in the range from 1200 to 2600 cm^{-1}, with both main polarizations of the incident light $E(\omega)\|z$ and $E(\omega)\|x$. Above a high-energy edge of the one-phonon spectra ≈1200 cm^{-1}, relatively intense features were observed, which can be assigned to multiphonon bands. The frequencies of the observed features differ for the two types of incident polarization. The features in the $E(\omega)\|z$ spectra are more narrow than in the $E(\omega)\|x$ spectra. It is natural to assume that the more intense features in this spectral range correspond to two-phonon absorption. In this case, the wave vector conservation rule allows participation of phonons with opposite **k** and −**k** vectors, throughout the Brillouin zone. In addition, the symmetry selection rules require that the direct product of irreducible representations for phonons involved contains the B_2 representation for the $E(\omega)\|z$ and the $E(x,y)$ representation for $E(\omega)\|x$ two-phonon spectra. A complete analysis of two-phonon spectra is out of the scope of this paper because it requires knowledge of phonon dispersion curves that remain unknown. Nevertheless, it is straightforward to list combinations of phonons with $k = 0$ at the Brillouin zone center that might result in two-phonon absorption features. Those are $(A_1 + B_2)$, $(A_2 + B_1)$, and $(E + E)$ pairs for the $E(\omega)\|z$ polarization and $(A_1 + E)$, $(A_2 + E)$, $(B_1 + E)$, and $(B_2 + E)$ pairs for the $E(\omega)\|x$ polarization. Since the number of phonon modes in copper metaborate is quite large, one might expect 220 features even for the $(A_1 + B_2)$ combination. 120 of these features are expected to lie in the spectral range of 1250–2200 cm^{-1}. Even taking into account only phonons with $k = 0$, one finds many combinations with sum frequencies close to the frequency of a particular feature in the multiphonon absorption spectra. For example, the following combinations of $k = 0$ phonons could contribute to the pronounced band at 1790 cm^{-1} [underlined in Fig. 7(a)] in the $E(\omega)\|z$ spectrum: $898(A_1) + 865(B_2$, LO); $596(A_1) + 1189(B_2$, LO); $725(A_1) + 1063(B_2)$; 560 (E, LO) + 1227(E, LO); 676 (E, TO) + 1122 (E, TO); etc.

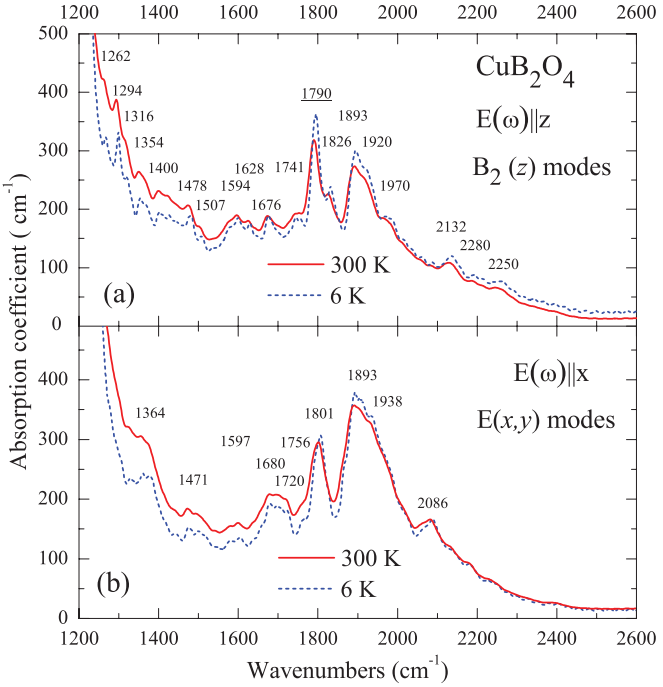

FIG. 7. (Color online) Multiphonon absorption spectra of CuB_2O_4 for the two polarizations of light $E(\omega)$ measured in a 104-μm thick sample at $T = 6$ and 300 K.

V. RAMAN SCATTERING SPECTRA

Symmetry analysis presented in Sec. II shows that $A_1(xx,yy,zz)$, $B_1(xx,yy)$, $B_2(xy,yx)$, and $E(xz,yz)$ types of the Raman active modes must be studied. We begin with the $x(zz)\bar{x}$ spectrum shown in Fig. 8. This spectrum is characterized by the highest intensity and the smallest number of the observed modes. In Table III, we summarize the experimental Raman data modes and compare them with $13A_1$ modes according to DFT calculations. The spectrum covers the range from the lowest mode at 250 cm^{-1} up to the highest mode at 1123 cm^{-1}. Symmetry analysis predicts $13A_1$

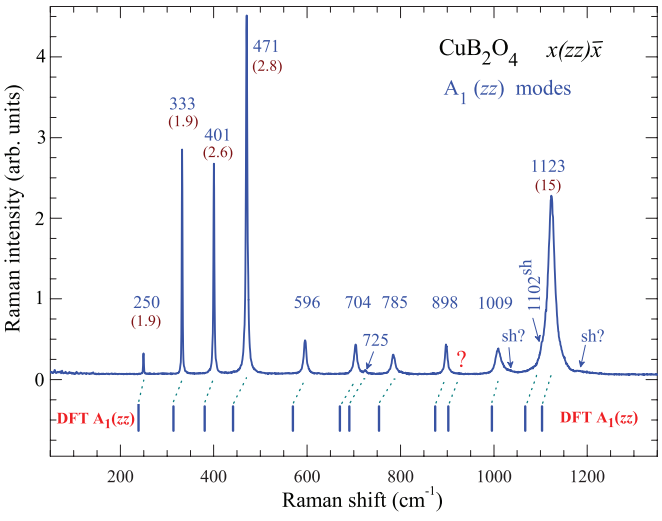

FIG. 8. (Color online) Raman scattering spectrum of CuB_2O_4 for the polarization $x(zz)\bar{x}$, which reflects the $A_1(zz)$ modes. Results of DFT calculations of the $A_1(zz)$ modes (see Sec. VI A) are shown in the lower part of the figure. In Table III, experimental data and DFT results are confronted. Numbers in brackets for several lines refer to the FWHM.

TABLE III. Experimental Raman frequencies of the $A_1(zz)$ modes as observed in the $x(zz)\bar{x}$ and $z(xx)\bar{z}$ spectra and computed DFT frequencies (see Sec. VI A). Column "Odds (%)" shows inequality between experimental and DFT frequencies. ("sh" stands for shoulder.)

	Frequency ω_j (cm^{-1})		
j	Raman A_1	DFT	Odds (%)
1	250	239.2	4.3
2	333	313.6	5.8
3	401	380.8	5.0
4	471	441.2	6.3
5	596	569.4	4.5
6	704	670.4	4.8
7	725	690.5	4.8
8	785	754.0	3.9
9	898	874.1	2.6
10	?	902.4	. . .
11	1009	995.5	1.3
12	$\approx$1102^{sh}	1067.2	3.2
13	1123[a]	1103.3	1.7

[a]In the $z(xx)\bar{z}$ spectrum, this line is observed at 1117 cm^{-1}.

modes for this choice of phonon propagation directions and polarizations, however, only 12 modes are reliably detected. The mode at 725 cm^{-1} has the lowest intensity in this spectrum but it was well reproduced in several samples with a different choice of experimental conditions (see, e.g., Fig. 9) thus making its existence unambiguous. A 1067.2 cm^{-1} DFT-calculated mode can be reliably assigned to a well pronounced shoulder at $\approx$1102 cm^{-1}. The only missing mode is a DFT mode at 902.4 cm^{-1}, which is marked by a question mark in Fig. 8. According to the general tendency of the shift

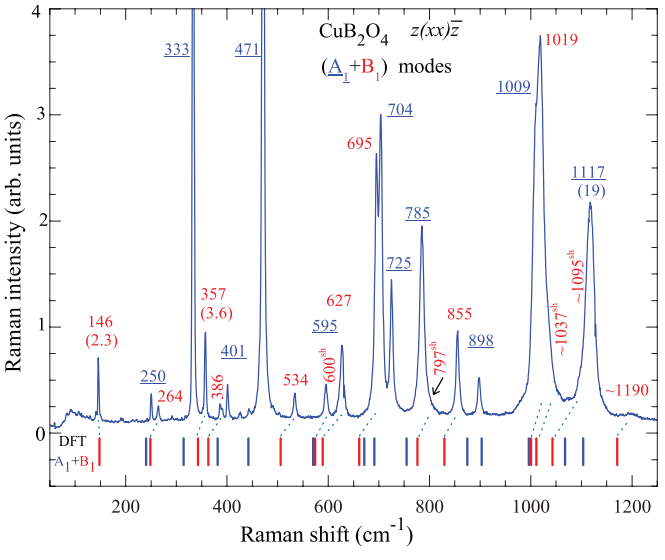

FIG. 9. (Color online) Raman scattering spectrum of CuB_2O_4 for the $z(xx)\bar{z}$ polarization, which reflects the $A_1(xx)$ and B_1(xx) modes. Blue underlined numbers show A_1 modes observed also in the $x(zz)\bar{x}$ spectrum in Fig. 8. Results of DFT calculations of the $A_1(zz)$ and $B_1(zz)$ modes (see Sec. VI A) are shown in the lower part of figure. Numbers in brackets for several lines refer to the FWHM.

between experimental data and DFT calculations (see Table III and Sec. VI), this mode is expected to be approximately at 920–940 cm^{-1}. However, no hint of any mode could be seen in this part of the spectrum. The observed $12A_1$ modes are presented graphically in Fig. 13 where modes of other symmetries are also summarized.

We would like to note that many lines in the Raman spectra of CuB_2O_4 for all modes are very narrow, on the order of $\approx$1 cm^{-1}, or even narrower because this value is approximately the resolution of our spectrometer. Such narrow Raman lines are not typical for transition-metal oxides. Moreover, as we noted above, very narrow lines with FWHM $\approx$ 1 cm^{-1} were observed in absorption spectra, e.g., a 503 cm^{-1} line in Fig. 6(d). In the $x(zz)\bar{x}$ Raman spectrum, the lowest frequency line at 250 cm^{-1} is the narrowest in the whole spectrum with FWHM = 1.6 cm^{-1}. A group of three intense lines is observed at 333, 401, and 471 cm^{-1}. The first one in this group is the narrowest with FWHM = 2.2 cm^{-1}. The characteristic feature of the spectrum is the most intense line at 471 cm^{-1} with FWHM = 2.8 cm^{-1}. In the high-energy range, one intense mode is observed at 1123 cm^{-1} with FWHM = 16.2 cm^{-1}.

Next, let us discuss the Raman spectra taken with (xx) and (yy) polarizations. These two polarizations produced identical spectra, as expected, and thus we discuss only the spectrum taken under $z(xx)\bar{z}$ geometry and polarization settings. In this case, the incident and scattered light propagates along the well defined z axis where the crystallographic birefringence vanishes. This spectrum is shown in Fig. 9. According to the symmetry analysis given in Sec. II, this spectrum should reflect $13A_1$ modes similar to those discussed in the previous paragraph and additionally $14B_1$ modes. $10A_1$ modes are observed at the same frequencies as in the $x(zz)\bar{x}$ spectrum shown in Fig. 8 (see Fig. 9, the first ten underlined numbers). However, in the high-frequency region, instead of the two A_1 modes observed at 1102 (shoulder) and 1123 cm^{-1} in the $x(zz)\bar{x}$ spectrum, only one strong line at 1117 cm^{-1} is observed in the $z(xx)\bar{z}$ Raman spectrum. Noting that the relative intensities of other A_1 modes are not the same in these two spectra, we suppose that the line at 1117 cm^{-1} results from the A_1 modes at 1102 and 1123 cm^{-1} having close intensities in the $z(xx)\bar{z}$ geometry. In the group of three intense A_1 lines at 333, 401, and 471 cm^{-1}, the middle one becomes strongly suppressed in the $z(xx)\bar{z}$ spectrum whereas the intensity of the 725 cm^{-1} line is strongly increased. All lines attributed to the A_1 modes in the $z(xx)\bar{z}$ spectrum are marked by underlined numbers. Other lines we attribute to the B_1 modes. In Table IV we summarize the experimental Raman data for the $14B_1$ modes and compare them with $14B_1$ modes according to DFT calculations (see Sec. VI A). Among these $14B_1$ modes, ten are well resolved and four are detected as well pronounced shoulders. The observed $14B_1$ modes are presented graphically in Fig. 13, along with modes of other symmetries.

Figure 10 shows the experimental $z(xy)\bar{z}$ Raman spectrum measured in the same geometry as the previous one in Fig. 8 for the incident and reflected scattered light propagating along the z axis but in crossed (xy) polarizations. This spectrum should reflect $17B_2$ LO modes. A characteristic feature of this spectrum is the strongest line at 265 cm^{-1} with FWHM = 3.8 cm^{-1}. Spectra in crossed (xy) polarizations are less intense, however, weak lines from other polarizations could be readily

TABLE IV. Experimental Raman frequencies of the $B_1(xx;yy)$ modes and the DFT-computed frequencies (see Sec. VI). Column "Odds(%)" shows inequality between experimental Raman and DFT frequencies. ("sh" stands for shoulder.)

	Frequency ω_j (cm^{-1})		
j	Raman B_1	DFT	Odds(%)
1	146	147.2	−0.8
2	264	247.7	6.3
3	357	341.6	4.3
4	386	362.3	6.1
5	534	505.2	5.4
6	≈600^{sh}	573.3	4.4
7	627	588.5	6.1
8	695	660.3	5.0
9	≈797^{sh}	775.3	2.7
10	855	828.8	3.1
11	1019	1000.0	1.9
12	≈1037^{sh}	1010.7	2.5
13	≈1095^{sh}	1042.5	4.8
14	1200	1170.5	2.5

identified when comparing all sets of the Raman spectra. Some of them are noted in Fig. 10. On the other hand, one gets important information from the infrared reflection and transmission data, which provide us with independent attribution and allow reliable identification of the $B_2(z)$ TO and LO modes. Good examples are the modes at 332 and 703 cm^{-1}. At a first glance, they could be attributed to the $A_1(xx)$ nonpolar modes seen in Figs. 8 and 9 at 333 and 704 cm^{-1}. We note that in the crossed $z(xy)\bar{z}$ polarizations these two lines are ≈1 cm^{-1} lower with respect to the A_1 lines. More important is their presence in the infrared reflection spectrum for $E(\omega)\|z$, thus, supporting their attribution to the $B_2(z)$ LO modes but not to leaks of A_1 or B_1 modes. Another example is a very weak mode at 110 cm^{-1} in the scattering spectrum, which is not observable in the reflection spectra but is readily observed in the infrared absorption spectra in a thick sample as seen in Fig. 6. We note that this mode at 110 cm^{-1} is the lowest frequency phonon because no other features were detected at lower frequencies down to 20 cm^{-1}. As a result, 17 lines in the Raman spectrum can be unambiguously assigned to the $B_2(z)$ LO modes in perfect agreement with 17 expected modes. They are summarized in Table I in comparison with the infrared data and DFT calculations. In most cases, agreement between frequencies of Raman lines and infrared LO phonons obtained by fitting is quite satisfactory.

Figure 11 shows the $y(xz)\bar{y}$ Raman spectrum, which should reflect the $E(x,y)$ LO modes. According to Eq. (1), this spectrum should contain 31 modes thus being characterized by the largest number of the observed modes in comparison to other spectra. A characteristic feature of this spectrum is the strongest line at 397 cm^{-1}. The lowest frequency line at 142 cm^{-1} shows FWHM = 1 cm^{-1}, which is the limit of spectral resolution of our spectrometer. We note that this spectrum shows the highest-frequency LO phonon at 1228 cm^{-1}. Some remarkable features of this Raman spectrum are several intense lines, which are practically unobservable in the reflection spectra and could be detected only in transmission spectra. Examples are the lines at 142 (FWHM = 1 cm^{-1}), 190 (FWHM = 1.6 cm^{-1}), 263, 360 cm^{-1}, and others (see Table II). On the other hand, several lines in the infrared spectra, such as 796, 915, 1086, and 1180 cm^{-1} can be hardly distinguished in the Raman spectra as weak shoulders in the vicinity of more intense lines. They are marked by arrows in Fig. 11.

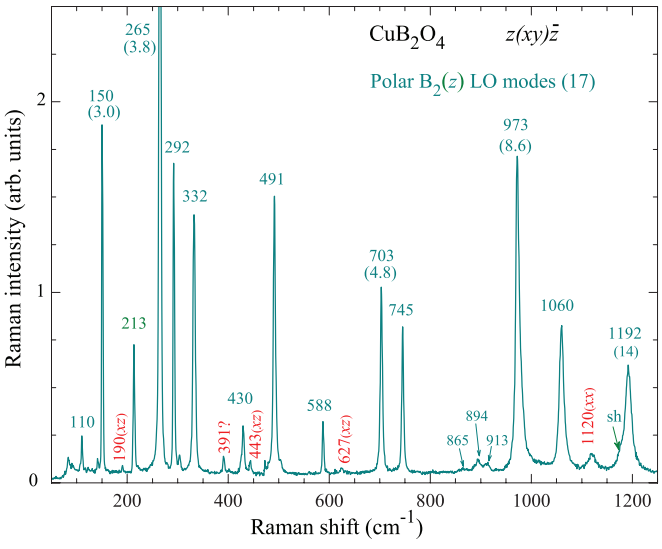

FIG. 10. (Color online) Raman scattering spectrum of CuB_2O_4 for the $z(xy)\bar{z}$ polarization, which reflects the polar $B_2(z)$ LO modes. Frequencies of these modes are given in Table I where we compare them with relevant frequencies obtained in infrared studies and in DFT calculations. Lines at 332 and 703 cm^{-1} with frequencies very close to those of the nonpolar A_1 and B_1 modes are nevertheless attributed to the $B_2(z)$ modes (see text). Several leaks from other polarizations are shown by red vertical numbers.

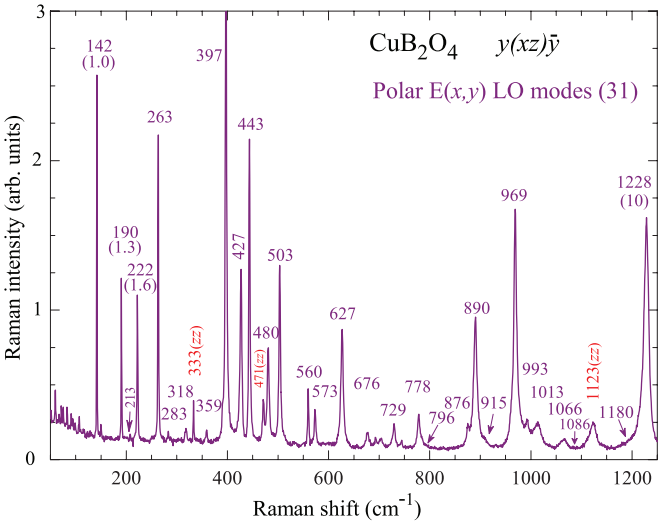

FIG. 11. (Color online) Raman scattering spectra of CuB_2O_4 for the polarization $y(zx)\bar{y}$, which reflects the $E(x,y)$ polar modes. Frequencies of these modes are given in Table II where we compare them with relevant frequencies obtained in infrared studies and in DFT calculations. Note a very narrow 1 cm^{-1} line at 142 cm^{-1}. Several leaks from other polarizations are noted in red by vertical numbers.

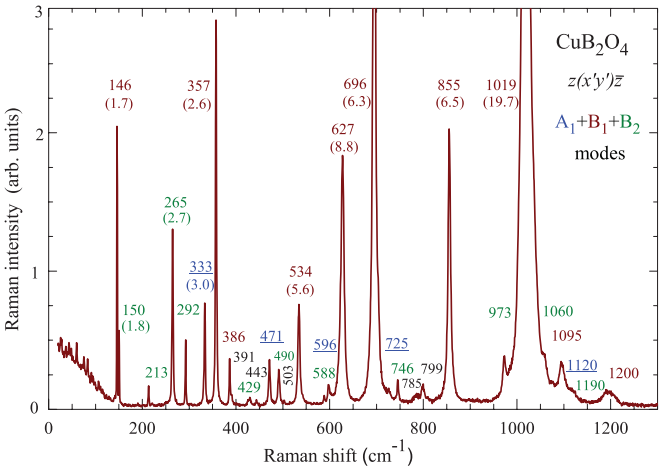

FIG. 12. (Color online) Mixed Raman scattering spectrum of CuB_2O_4 for the polarization $z(x'y')\bar{z}$ (see text), which reflects the sum of A_1, B_1, and B_2 modes.

In order to make more reliable assignments of the Raman lines, we performed supplementary measurements using mixed polarizations. Figure 12 shows a Raman spectrum measured for the $z(x'y')\bar{z}$ polarization where x' and y' axes are rotated by 45° with respect to the x and y axes around the z axis of the crystallographic unit cell. This mixed spectrum shows the presence of A_1, B_1, and B_2 modes. For example, in the low-frequency region, we see a B_1 mode at 146 cm^{-1} and a B_2 mode at 151 cm^{-1}, whereas in the proper polarizations only one or another lines are observed. Though in the tetragonal crystal, the (xy) plane is optically isotropic, it is important to remind, and we observed in many measurements, that the Raman spectra are very sensitive to small misalignments of the incident/scattered polarizations with respect the equivalent x and y axis, and obviously with respect to the z axis. The ratio between intensities in the mixed spectra can be varied by changing the angle between crystallographic axes and polarization of the exciting/scattered light. Obviously, another important factor was precise orientation of the sample faces.

Figure 13 graphically summarizes experimental infrared and Raman data for nonpolar A_1, B_1, and polar B_2, and E modes. In Table V, we summarize numerically the Raman data obtained with five orientation-polarization settings as it was described in this section.

TABLE V. Summary of the Raman spectra measured with five different settings. Raman modes and their presence in each of the setting are shown. Numbers in brackets in the first line show the number of expected modes (see Sec. II). Numbers in lines 2 to 5 show numbers of experimentally detected modes shown in columns 2 to 5.

Geometry	$A_1(13)$	$B_1(14)$	$B_2(z)(17)$	$E(x,y)(31)$
$x(zz)\bar{x}$	11	. . .	. . .	. . .
$z(xx)\bar{z}$	11	14	. . .	. . .
$z(xy)\bar{z}$	. . .	. . .	17	. . .
$y(xz)\bar{y}$	. . .	. . .	. . .	30
$z(x'y')\bar{z}$	11	14	17	. . .

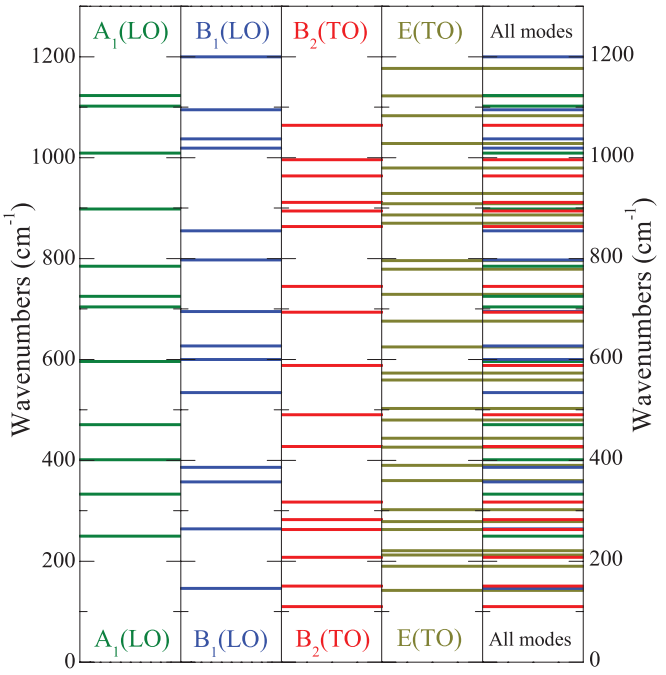

FIG. 13. (Color online) Comparative summary of the A_1, B_1, B_2, and E modes observed in CuB_2O_4 in infrared reflection and absorption spectra, and Raman scattering spectra.

VI. *AB INITIO* CALCULATIONS OF THE VIBRATIONAL MODES

A. Nonpolar A_1 and B_1 modes

According to Eq. (2), A_1 modes are active in the Raman spectra with (xx), (yy), and (zz) polarizations whereas B_1 modes are active with (xx) or (yy) polarization. These spectra are shown in Figs. 8 and 9 where Raman data are compared with the results of DFT calculations. Dotted lines in these figures show tentative assignments which seem to be quite reasonable for the A_1 modes in the low-frequency region. The best numerical correspondence is observed for the lowest mode, which is at 250 cm^{-1} in experiment and 239.2 cm^{-1} in calculations. In fact, there is unequivocally one-to-one correspondence between the theoretical line distribution and line positions in experimental spectra, even if the computed frequencies are systematically lower by about 30 cm^{-1}. At higher frequencies, above 600 cm^{-1}, there are eight computed lines but only seven spectral lines are observed. Only one mode at 902.4 cm^{-1} according to DFT calculations is lacking. This lack may be attributed to its low intensity. Experimental Raman and computed frequencies of the A_1 modes are collected in Table III. The last column in this table shows the inequality between experimental and DFT data for each mode.

By extracting from the $z(xx)\bar{z}$ spectrum the lines observed in the $x(zz)\bar{x}$ spectrum, one discriminates the lines related to the B_1 modes. Tentative assignment of these modes is shown in the lower part of Fig. 9. Experimental Raman and computed frequencies of the B_1 modes are collected in Table IV. Again, we note that the best numerical correspondence is observed for the lowest mode at 146 cm^{-1} in experiment and 147.2 cm^{-1} in calculations. The divergence between theory and experiment in this table suffers the same general discrepancy; namely, for

the most part, the computed frequencies are lower than the experimental ones on the average by ≈25 cm^{-1}.

B. Polar $B_2(z)$ modes polarized along the tetragonal z axis

The $B_2(z)$ modes are polarized along the z axis and are active in the Raman spectra with the (xy) polarization. Thus, only the $B_2(z)$ LO modes contribute to the $z(xy)\bar{z}$ Raman spectrum. Unfortunately, our computational facilities allow calculations of only TO modes and therefore we are unable to make a direct comparison of the $z(xy)\bar{z}$ Raman spectrum with the computational results. However, we can compare the computed frequencies of the $B_2(z)$ TO modes with the positions of singularities in the infrared reflectance spectrum registered in the $E(\omega)\|z$ setting as it is shown in Fig. 5 and in Table I. We should note an exact coincidence between the number of computed modes and the observed spectral lines within all frequency intervals. It is remarkable to note that according to Table I the lowest experimentally observed $B_2(z)$ mode in Raman and infrared studies is at 110 cm^{-1} whereas it is at 108 cm^{-1} in the DFT calculations. At higher frequencies, as in the case of the nonpolar modes, there is a systematic discrepancy, namely, the computed frequencies are lower than the experimental ones by 30 cm^{-1} on the average.

We have made an attempt to confirm these assignments by analyzing the infrared intensities. Oscillator strengths were obtained from fitting the experimental reflectance spectrum within the harmonic oscillator model. Theoretical estimates of the infrared intensities were done within a rigid ion model with formal ionic charges $q(O) = -2e$, $q(B) = +3e$, and $q(Cu) = +2e$. Analysis of intensities in the infrared spectra allows us to select the most intense polar $B_2(z)$ modes. According to our computations, there are four such modes, all positioned within the high-frequency interval of 900–1100 cm^{-1}. This conclusion is in line with experimental data. At the same time, experiment reveals one additional intense line at 694 cm^{-1} in the infrared spectrum [see Fig. 5(a)] and at 703 cm^{-1} in the Raman spectrum (see Fig. 11). However, no such prominent mode could be found in the computed spectrum. We assume that this discrepancy might indicate inadequacy of the rigid ion model below the high-frequency region.

C. Polar $E(x,y)$ modes polarized along the x axis

The $E(x,y)$ modes are polarized in the (xy) plane and therefore they contribute to the infrared reflectance spectrum registered in the $E(\omega)\|x$ setting. Besides, the $E(x,y)$ modes are Raman active. Those polarized along the x axis are active in the Raman spectra with (xz) polarization, and those polarized along the y axis are active with the (yz) polarization. Therefore Raman spectra recorded in the $y(xz)\bar{y}$ and $x(zy)\bar{x}$ settings both are related to the $E(x,y)$ LO modes. The infrared reflectance spectrum recorded in the $E(\omega)\|x$ setting is shown in Fig. 5(b) in comparison with the computed frequency distribution of the $E(x,y)$ TO modes. Corresponding numerical values are presented in Table II.

Dotted lines in Fig. 5(b) show tentative assignment for the $E(x,y)$ modes. Table II shows results of experiments and calculations. The assignment is more or less evident within the whole frequency interval. The problem aggravates in the high-frequency range, which includes the most intense phonons. To overcome this difficulty, we have estimated infrared intensities of the $E(x,y)$ modes by using the same rigid ion model discussed above. This analysis allows us to select the most polar $E(x,y)$ modes and correlate them with the most prominent spectral features.

VII. DISCUSSION

The experimental infrared and Raman data and the calculated DFT frequencies of all zone-center modes are summarized in Tables I–IV and presented graphically in Figs. 13 and 14. In Table I, we see a very good agreement of the order of 1–2% between the first three low-frequency experimental and calculated $B_2(z)$ modes. The difference increases for the modes of higher frequency and on the average it is 3.3% when all modes are taken into account. Analysis of the difference between experimental and DFT data in Table II gives the inequality of 3.7%. In Tables III and IV, the odds between experimental and DFT data are shown for each mode in the last column. On the average, the odds are 3.7% and 4.0% for A_1 and B_2 modes, respectively.

Conventionally, the frequency distribution of phonons over the whole spectral range can be divided into several zones. They are labeled by majuscule Roman numbers I to V at the top of Fig. 14. Their borders and numbers of modes are 1170–829 cm^{-1} (44 modes), 775–750 cm^{-1} (six modes), 710–649 cm^{-1} (nine modes), 605–239 cm^{-1} (49 modes), and 210–108 cm^{-1} (15 modes) for zones I–V, respectively. Trying to rationalize this frequency distribution we turn to the internal modes of the BO_4 tetrahedron, which are the basic units of the crystal lattice. Frequencies of these modes in an isolated BO_4 tetrahedron are discussed in Sec. II and shown in Fig. 13.

Three modes of the highest frequency involve predominantly oscillations of boron atoms around their positions at the centers of tetrahedrons. There are twelve BO_4 tetrahedrons per unit cell. Correspondingly, the vibrational spectrum of

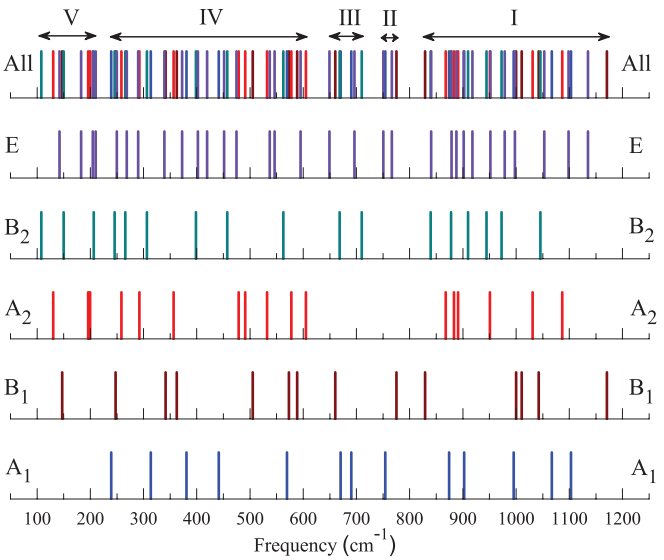

FIG. 14. (Color online) Frequency distribution of all five types of the zone-center modes according to DFT calculations. The A_2 modes are neither infrared nor Raman active.

CuB_2O_4 must contain 36 such modes. Evidently, these modes must belong to zone I. The large frequency range of zone I might be certainly related to a wide scatter of the B-O bond lengths from 1.444 to 1.487 Å.

Taking into account the frequencies of normal modes of the BO_4 tetrahedron, zone II must contain the modes related to ν_1 vibrations. That is a pulsation mode, which involves a synchronous stretching of all B-O bonds. In the framework lattice of the CuB_2O_4 crystal, the tetrahedrons are linked by common apexes. This imposes some constraints on the vibrations predominantly augmenting their frequencies. This structural peculiarity may cause "migration" of several ν_1 modes from zone II to zone I. In total, zones I and II should contain 48 modes. They must be separated presumably by a rather wide gap of about 200 cm^{-1} from the lower zones of the spectrum. However, the calculated frequency distribution corresponds to 50 modes and does not confirm a presence of such a wide gap. Hence, there should be another factor for augmenting frequencies of the ν_4 and ν_2 modes. Evidently, these are the Cu-O interactions. To verify this hypothesis, we have analyzed the calculated eigenvectors representing them in terms of the bond-length variations. Amplitudes of such variations averaged over the unit cell for the B-O and Cu-O bonds are shown in Fig. 15. Note the difference in scales between the panels in this figure. Evidently, the largest amplitudes are for the boron atoms.

It can be seen that all modes with frequencies above 900 cm^{-1} involve quite insignificant variations of the Cu-O bonds. Therefore these modes can be referred to as pure B-O stretching vibration. While approaching the low-frequency border of zone I down to 830 cm^{-1}, variations of the Cu-O bond amplitudes are markedly augmented. The relevant modes can no longer be classified as pure bond stretching vibrations of the boron-oxide framework. The effect of the Cu-O interactions results in mixing and augmentation of the frequencies of these modes.

The largest Cu-O bond amplitudes are inherent to the modes within zones II and III. This result confirms our hypothesis about the origin of the systematic blue frequency shift of experimental modes with respect to calculated ones in the middle part of the vibrational spectrum of CuB_2O_4. Namely, this shift is due to the presence of copper atoms, which makes the boron-oxide tetrahedrons elastically harder with respect to many normal middle-range vibrations. It should be emphasized that cooper atoms do not oscillate within these modes. This is evidenced by the calculated atomic amplitudes for Cu(4*b*) and Cu(8*d*) atoms shown in two upper panels (a) and (b) in Fig. 16.

One can see that amplitudes of both Cu(4*b*) and Cu(8*d*) atoms are very small for the modes above 300 cm^{-1}, but they are considerable for the modes around and below 200 cm^{-1}. Moreover, there are four modes that can be considered as characteristic modes of Cu(4*b*) atoms. Two such modes of the $E(x,y)$ type with DFT frequencies 204 and 210 cm^{-1} involve the Cu(4*b*) oscillation in the (xy) plane, two others of the $B_1(xx)$ and $B_2(z)$ types with DFT frequencies 147 and 149 cm^{-1} involve the Cu(4*b*) oscillations along the z axis. These modes almost do not mix with other types of vibrations. The presence of such perfectly localized modes is due to specific positions of Cu(4*b*) atoms at the centers of planar squares. By contrast, there are no such modes for the Cu(8*d*) atoms.

The discussed above modes correspond to the experimentally observed E(*x,y*) modes at 212 and 221 cm^{-1} and $B_1(xx)$ and $B_2(z)$ modes at 146 and 151 cm^{-1}, respectively (see Tables I, II, and IV). The members of each pair of these modes have close frequencies, which enables to interpret them as

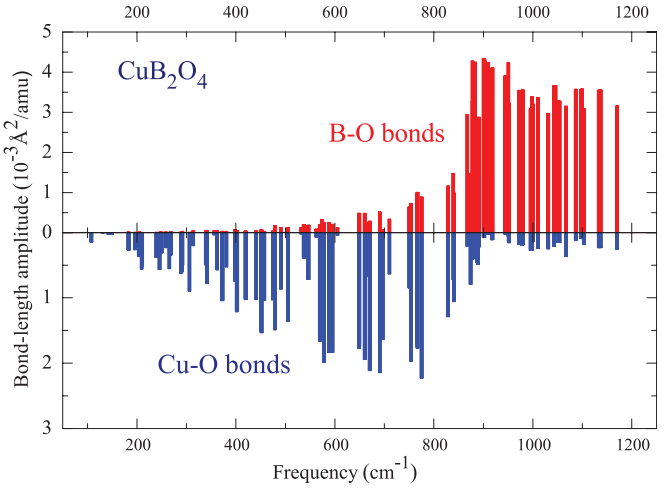

FIG. 15. (Color online) Average per unit cell square amplitudes of B-O and Cu-O bond-length variation vs normal mode frequency.

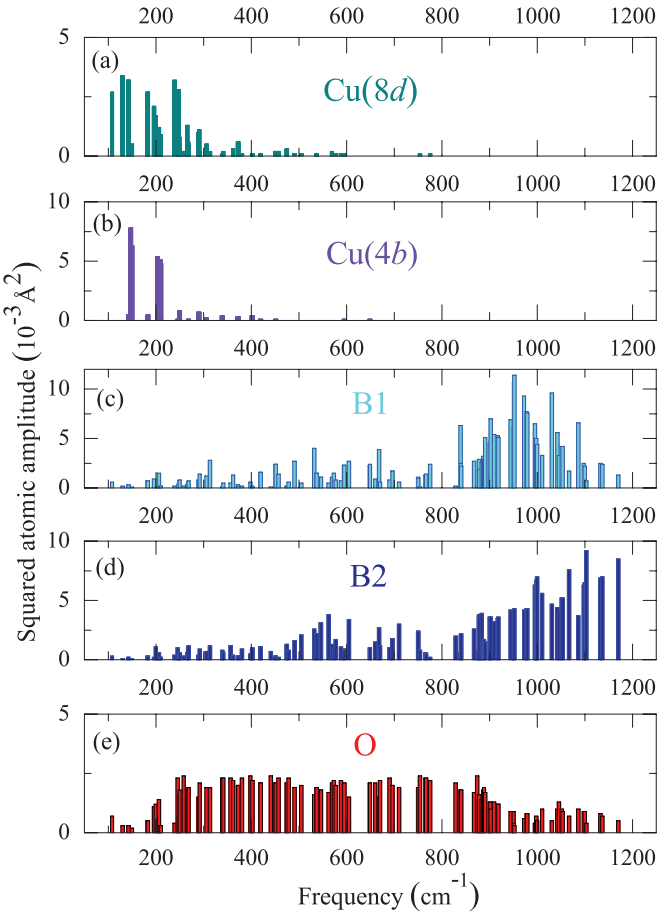

FIG. 16. (Color online) Average per unit cell squared amplitudes of different atoms vs normal mode frequency.

TABLE VI. Observed groups of crystal vibrational modes with close frequencies and their tentative assignment to Davydov multiplets originating from vibrations of the $Cu(4b)O_4$ and $Cu(8d)O_4$ units in the structure of CuB_2O_4.

$4b(S_4)$		$8d(C_2)$		
$3(B_1+B_2)$	$4*2E$	$3(A_1+B_1+E)$	$4(B_2+E+[A_2])$	$4(A_1+B_1+B_2+2E+[A_2])$
146 + 151	**212 + 221**	401 + 386 + 390	428 + 426	250 + 264.4 + 263.2 + 263 + 279
695 + 694	559 + 573	596 + 627 + 625	491 + 503	333 + 332 + 357 + 359 + 318
855 + 863	779 + 796	1123 + 1095 + 1122	*863 + 870*	704 + *695* + *694* + 676 + 729
1037 + 1064	*870 + 886*		894 + *886*	898 + *855* + *863* + *870* + *886*

Davydov doublets originating from oscillations of the copper atom residing at the center of the $Cu(4b)O_4$ molecular unit (see Sec. II C). Inspection of Tables I–IV shows that also other pairs, groups of three and even five close frequencies are observed in the spectra. Figure 13 illustrates this statement. Table VI summarizes the observed groups of modes and gives their tentative assignment to Davydov multiplets originating from vibrations of the $Cu(4b)O_4$ and $Cu(8d)O_4$ units in the structure of CuB_2O_4. The above discussed doublets at $(212+221)$ and $(146+151)$ cm^{-1} are indicated in bold. Frequencies of modes that could be put into different columns of Table VI are in italics. One has to keep in mind that Cu-O vibrations with frequencies higher than 900 cm^{-1} are strongly mixed with B-O vibrations.

VIII. CONCLUSIONS

The results presented in this paper show a very rich structure of phonons in CuB_2O_4, revealed by polarized infrared reflection and transmission spectra and by Raman scattering spectra. In accordance with the symmetry analysis, infrared studies allowed us to detect all polar $17B_2(z)$- and $31E(x,y)$-type normal vibrational modes. Several very weak phonon polar modes were not detectable in the reflection experiments but were reliably observed in the absorption experiments using 104 and 784-μm thick samples. The dispersion analysis has been applied to the infrared reflectance data, and the frequencies of longitudinal (LO) and transverse (TO) optical phonons at the center of the Brillouin zone were obtained using the Lorentz model of attenuated oscillators. Raman scattering spectra allowed us to determine the LO phonons belonging to the polar $B_2(z)$, and the $E(x,y)$ modes and the obtained frequencies are consistent with the infrared results. The frequencies of the majority of nonpolar $A_1(xx,yy,zz)$ and $B_1(xx,yy)$ modes were obtained from the Raman scattering spectra. Several groups of observed closely spaced modes were assigned to Davydov multiplets originating from the interaction between several CuO_4 molecular units present in the primitive crystallographic cell of CuB_2O_4.

We applied the density functional theory for simulating the atomic structure and calculating vibrational frequencies of CuB_2O_4. The computed frequency distribution was found to be consistent with the observed line positions in infrared and Raman spectra. In particular, a very good agreement is present for the lowest frequency modes, as can be seen in Tables I–IV. For the modes of higher frequencies, a systematic shift between experimental and computed frequencies is observed. On the average, the difference between experimental and DFT phonon frequencies lies between 3.3% [$B_2(z)$ modes] and 4.0% [$B_1(xx)$ modes] that can be regarded as a satisfactory result for such a complex material with a huge amount of polar and nonpolar phonons. This allowed us to attribute all prominent spectral features to zone-center phonons of particular symmetries and to particular atomic displacements. Estimates of the infrared intensities performed within a rigid ion model allowed selecting the most intense infrared active modes. These estimates provide an additional justification of the suggested phonon assignments.

In summary, all experimental and theoretical results and their analysis presented in this paper have provided a reliable identification of all zone-center phonon modes in CuB_2O_4, a compound with a complex crystal structure, demonstrating a rich variety of interesting magnetic, optical and magneto-optical properties. We believe that these results constitute a firm basis for further studies of not only the lattice dynamics of this material but also of its magnetic, electronic, optical, and magneto-optical properties. In particular, we are convinced that our results will serve as absolutely necessary information for interpreting unique vibronic spectra reported in previous publications but which could not be subjected to any serious analysis without knowledge of the phonon spectra.

ACKNOWLEDGMENTS

This work was supported by the Russian Ministry for Education and Science (project 14.B25.31.0025), the Russian Foundation for Basic Research (project 12-02-00130a), the Russian Academy of Sciences under the Programs for Basic Research and the President of Russian Federation (project MK-1700.2013.2). R.V.P. thanks A. M. Kalashnikova for the help in the preparation of the manuscript.

[1]D. I. Mendeleev, *Fundamentals of Chemistry* (in Russian, St. Petersburg, 1909). In this book, D. I. Mendeleev cites a succesful synthesis of $CuOB^2O^3$, $NiOB^2O^3$, and some other borates by a German metallurgist W. M. Guertler.

[2]M. Martinez-Ripoll, S. Martinez-Carrera, and S. Garcia-Blanco, Acta Cryst. B **27**, 677 (1971).

[3]G. K. Abdullaev and K. S. Mamedov, J. Struct. Chem. **22**, 637 (1981).

[4]J. Schlueter, D. Pohl, and U. Golla-Shindler, Neues Jahrb. Mineral., Abh. **185**, 27 (2008).
[5]M. Boehm, B. Roessli, J. Schefer, A. Wills, B. Ouladdiaf, E. Lelievre-Berna, U. Staub, G.A. Petrakovskii, Phys. Rev. B **68**, 024405 (2003).
[6]B. Roessli, J. Schefer, G. Petrakovskii, B. Ouladdiaf, M. Boehm, U. Staub, A. Vorotinov, L. Bezmaternikh, Phys. Rev. Lett. **86**, 1885 (2001).
[7]M. Boehm, B. Roessli, J. Schefer, A. Amato, C. Baines, U. Staub, and G. Petrakovskii, Physica B - Condens. Matter **318**, 277 (2002).
[8]A. I. Pankrats, G. A. Petrakovskii, M. A. Popov, K. A. Sablina, L. A. Prozorova, S. S. Sosin, H. Szimczak, R. Szimczak, and M. Baran, JETP Lett. **78**, 569 (2003).
[9]G. Nenert, L. N. Bezmaternykh, A. N. Vasiliev, T. T. M. Palstra, Phys. Rev. B **76**, 144401 (2007).
[10]J. N. Hancock, G. Chabot-Couture, Y. Li, G. A. Petrakovskiui, K. Ishii, I. Jarrige, J. Mizuki, T. P. Devereaux, and M. Greven, Phys. Rev. B **80**, 092509 (2009).
[11]K. S. Aleksandrov, B. P. Sorokin, D. A. Glushkov, L. N. Bezmaternykh, S. I. Burkov, and S. V. Belushchenko, Phys. Solid State **45**, 42 (2003).
[12]Y. Kousuka, S.-I. Yano, J.-I. Kishine, Y. Yoshida, K. Inoue, K. Kikuchi, and J. Akimitsu, J. Phys. Soc. Jpn. **76**, 123709 (2007).
[13]M. A. Popov, G. A. Petrakovskii, and V. I. Zinenko, Phys. Solid State **46**, 491 (2004).
[14]S. N. Martynov, J. Exp. Theor. Phys. **109**, 979 (2009).
[15]Y. Yasuda, H. Nakamura, Y. Fujii, H. Kikuchi, M. Chiba, Y. Yamamoto, H. Hori, G. Petrakovskii, M. Popov, and L. Bezmaternikh, J. Phys.- Condens. Matter **19**, 145277 (2007).
[16]M. Fiebig, I. Sänger, and R. V. Pisarev, J. Appl. Phys. **93**, 6960 (2003).
[17]S. Martynov, G. Petrakovskii, M. Boehm, B. Roessli, and J. Kulda, J. Magn. Magn. Mater. **299**, 75 (2006).
[18]N. N. Nesterova, R. V. Pisarev, and G. T. Andreeva, Phys. Status Solidi B **65**, 103 (1974).
[19]R. V. Pisarev, A. M. Kalashnikova, O. Schöps, and L. N. Bezmaternykh, Phys. Rev. B **84**, 075160 (2011).
[20]M. Saito, K. Ishikawa, K. Taniguchi, T. Arima, Phys. Rev. Lett. **101**, 117402 (2008).
[21]T. Arima, J. Phys.: Condens. Matter **20**, 434211 (2008).
[22]S. W. Lovesey and U. Staub, J. Phys.: Condens. Matter **21**, 142201 (2009).
[23]T. Arima and M. Saito, J. Phys.: Condens. Matter **21**, 498001 (2009).
[24]S. W. Lovesey and U. Staub, J. Phys.: Condens. Matter **21**, 498002 (2009).
[25]R. V. Pisarev, I. Sänger, G. A. Petrakovskii, and M. Fiebig, Phys. Rev. Lett. **93**, 037204 (2004).
[26]M. Fiebig, V. V. Pavlov, and R. V. Pisarev, J. Opt. Soc. Amer. **22**, 96 (2005).
[27]R. V. Pisarev, J. Lumin. **133**, 169 (2013).
[28]J. Liu, S. Wen, X. Zou, F. Zou, G. J. O. Beran, and P. Feng, J. Mater. Chem. A **1**, 1553 (2013).
[29]L. V. Udod, K. A. Sablina, Y. N. Ivanov, G. A. Petrakovskii, A. Y. Koretz, and A. F. Bovina, Phys. Met. Metallogr. **100**, S39 (2005).
[30]Th. Hahn, Editor, *International Tables for Crystallography: Space-Group Symmetry*, 5th ed. (Springer, Dordrecht, The Netherlands, 2005), Vol. A.
[31]D. J. Rousseau, R. P. Bauman, and S. P. S. Porto, J. Raman Spectrosc. **10**, 253 (1981).
[32]M. I. Aroyo, J. M. Perez-Mato, D. Orobengoa, E. Tasci, G. de la Flor, and A. Kirov, *Crystallography online: Bilbao Crystallographic Server*, Bulg. Chem. Commun. **43**, 183 (2011).
[33]K. Nakamoto, *Infrared and Raman Spectra of Inorganic and Coordination Compounds* (Wiley, New York, 1986).
[34]A. S. Davydov, *Theory of Molecular Excitons* (McGraw-Hill, New York, 1962).
[35]G. K. Abdullaev, P. F. Rzazade, and S. H. Mamedov, Zh. Neorg. Khim. **27**, 1837 (1982).
[36]R. G. Parr and W. Yang, *Density-Functional Theory of Atoms and Molecules* (Oxford University Press, New York, 1989).
[37]R. Dreizler and E. Gross, *Density Functional Theory* (Plenum Press, New York, 1995).
[38]W. Koch and M. C. Holthausen, *A Chemist's Guide to Density Functional Theory* (Wiley-VCH, Weinheim, 2002).
[39]B. Delley, J. Chem. Phys. **113**, 7756 (2000).
[40]J. P. Perdew and Y. Wang, Phys. Rev. B **45**, 13244 (1992).
[41]B. Delley, J. Chem. Phys. **92**, 508 (1990).
[42]D. Fausti, A. A. Nugroho, P. H. M. van Loosdrecht, S. A. Klimin, M. N. Popova, and L. N. Bezmaternykh, Phys. Rev. B **74**, 024403 (2006).
[43]A. B. Kuzmenko, D. van der Marel, P. J. M. van Bentum, E. A. Tishchenko, C. Presura, A. A. Bush, Phys. Rev. B **63**, 094303 (2001).